A terahertz view on magnetization dynamics

Awari, Nilesh

CHAPTER 3

Experimental Techniques

This thesis focuses on questions related to magnetization dynamics involving THz pulses either for excitation or as a sensitive probe. Here, the experimental techniques and instruments employed to address the questions in the following chapters are discussed as follows:

- *THz emission spectroscopy (TES) is a technique used to measure the magnetic properties of ultra-thin films (Chapter 4). The ferromagnetic resonance (FM) for $Mn_{3-X}Ga$ thin films is in the range of 0.1 - 0.4 THz, which are studied using TES. In this frequency range, TES proved to be a more sensitive technique as compared to all optical ultra-fast magneto-optical techniques.*
- *Chapter 5 of the thesis deals with THz induced demagnetization of amorphous CoFeB thin films. Here we use the ability of THz radiation to generate spin-polarized current in ferromagnetic thin films and its effect on ultra-fast demagnetization is studied using the polar magneto-optical Kerr effect.*
- *Chapter 6 of the thesis discusses the THz coherent control of antiferromagnetic (AFM) mode of the single crystalline NiO. The AFM mode of the NiO is selectively excited using a narrow band THz pump and it is probed using the Faraday effect.*

3.1 THz emission spectroscopy

Terahertz (THz) emission spectroscopy is a technique based on the coherent detection of flashes of THz light emitted when intense ultra-short photon pulses interact with matter. The first demonstration of radiation emitted in this way was in 1990 when it was observed as a result of free carrier excitation and optical rectification in semiconductors [1]. The emitted pulses were broadband, and carried information on carrier relaxation time, phonon absorption, and/or the electro-optical coefficients. Since then, this technique has been used to study a multitude of materials for their different ultra-fast dynamics. In 2004, it was discovered that laser-driven demagnetization processes can give rise to broadband, single-cycle THz pulse emission [2, 3]. In that case, the spectrum of the emitted burst carries information on the time-scale of the demagnetization process, making THz emission spectroscopy a powerful diagnostic technique for studying laser-driven ultra-fast non-equilibrium dynamics in matter. In 2013, the method was successfully applied to determine the duration of ultra-fast laser-driven spin currents [4]. Most recently, researchers have succeeded in detecting narrow-band emission from spin waves in ferrimagnetic bulk insulators [5, 6] and antiferromagnetic insulators [7].

In this study TES is emplyed to study the FM modes in $Mn_{3-X}Ga$. The THz emission from these materials is based on magnetic dipole emission. The electromagnetic radiation is emitted when a magnetic dipole oscillates in time. Using vector potentials for a circulating current loop one can find the electric field (E_t) emitted from such a loop [8] as:

$$\boldsymbol{E}_t = \frac{-\delta \boldsymbol{A}}{\delta t} \sim \frac{\delta[\boldsymbol{m} \times \hat{n}]}{\delta t} \tag{3.1}$$

where $\boldsymbol{m}$ is the magnetic dipole moment, $\boldsymbol{A}$ is vector potential and $\hat{n}$ is the radial unit vector for circulating motion. In the case of $Mn_{3-X}Ga$, the emission is from multiple magnetic dipoles which are oscillating in a coherent fashion at the frequency of the ferromagnetic resonance (FMR) upon excitation by ultra-fast laser pulses with a pulse duration shorter than the magnetization oscillation, as discussed in chapter 4. For such cases, the far-field radiation is diffraction limited and given by the following equation [9],

$$E_t \sim \mathrm{sinc}(\pi d(\sin\theta)/\lambda)^2 \tag{3.2}$$

where d is the laser spot size on the sample, λ is the wavelength of the emitted radiation and θ is the angle between the surface normal and the observation angle.

3.1.1 Electro-Optic Sampling

The detection technique for freely propagating THz radiation used in this work is based on electro-optic (EO) sampling [10–12]. The linear EO effect, also known as the Pockels effect, describes birefringence induced in electro-optic material in response to an applied electric field. This effect is observed in materials with broken inversion symmetry. EO detection allows simultaneous detection of phase and amplitude of the THz electric field.

In the presence of the THz electric field, EO material becomes birefringence. This birefringence is proportional to the THz electric field and can be probed with collinearly propagating short near infrared 800 nm probe pulses. The probe pulse experience the transient birefringence and changes its polarization state which can be detected using a balanced detection scheme. A balanced detection scheme consists of a $\frac{\lambda}{4}$ wave-plate for probe wavelength, a Wollaston prism (WP) and, a pair of balanced photo-diodes (PD), see Figure 3.1. In the absence of a THz electric field, a linear probe beam becomes circularly polarized because of the $\frac{\lambda}{4}$ wave-plate. WP separates two orthogonal polarizations from the circularly polarized probe beam and they are balanced on the photo-diodes. When the THz electric field is present, ellipticity in probe beam is induced in the EO material, which unbalances the photo-diode signal. This unbalanced photo-diode signal is a measure of the THz electric field.

For collinear EO sampling in a material of thickness L, the differential phase retardation, which is a measure of the THz electric field, is given by [13],

$$\delta\phi(t) = \frac{2\pi L n_0^3 r}{\lambda} E(t) \tag{3.3}$$

Here r is the EO coefficient of the detector material, E is the electric field of the THz radiation, and n_0 is the unperturbed refractive index. The complete mapping of the THz electric field transient can be done by delaying the probe beam with respect to the THz beam. This equation assumes perfect phase matching between the group velocity of the 800 nm probe beam and the phase velocity of the THz beam.

In this thesis, a ZnTe crystal cut along the <110> crystallographic direction is used for THz detection. ZnTe is an isotropic crystal having a zincblende structure with non-zero EO coefficients along the r_{41}, r_{52}, and r_{63} directions.

The THz detection efficiency decreases as the velocity mismatch between two beams increases. Therefore it is important to optimize the thickness of the ZnTe crystal for the efficient detection of the THz frequency under consideration. The minimum distance

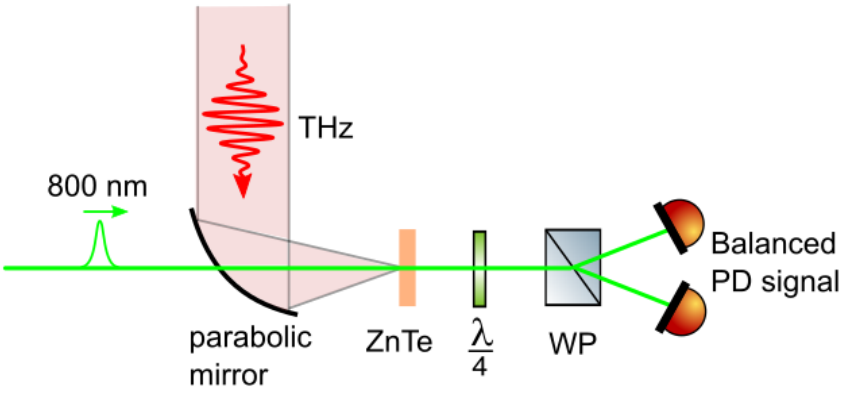

FIGURE 3.1: Schematic of the electro-optic set-up used in this thesis. The THz radiation pulses (shown in red) are focused on the electro-optic crystal (ZnTe) and 800 nm NIR laser pulses (shown in green) are collinear with the THz pulses. The THz field induces birefringence in the electro-optic crystal, the differences in the orthogonal polarization is detected using a quarter-wave plate ($\frac{\lambda}{4}$), a Wollaston prism (WP) and a pair of photo-diodes (PD).

over which velocity mismatch can be tolerated for THz detection is called the coherence length, defined as

$$l_c(\omega_{THz}) = \frac{\pi c}{\omega_{THz}|n_{opt}(\omega_0) - n_{\mathrm{THz}}(\omega_{THz})|} \tag{3.4}$$

where, n_{opt} is the refractive index of the probe pulse inside the ZnTe crystal along the <110> direction and n_{THz} is the refractive index of THz radiation in ZnTe crystal along the same crystallographic axis.

3.2 Magneto-optic effect

Magneto-optical effects are the result of the interaction of light and matter when the latter is subject to a magnetic field. For some magnetically ordered materials, such as ferromagnets, ferrimagnets etc, magneto-optical effects are present even in the absence of an externally applied magnetic field. In magneto-optical effects, the polarization of the incident light rotates after interacting with magnetization of the materials [14, 15].

For the analysis of the magneto-optic Kerr effect [16] and other phenomena in detail, consider the isotropic media having a permittivity tensor as written below:

$$\epsilon = \begin{pmatrix} \epsilon_{xx} & 0 & 0 \\ 0 & \epsilon_{yy} & 0 \\ 0 & 0 & \epsilon_{zz} \end{pmatrix} \tag{3.5}$$

When an external magnetic field is applied parallel to the direction of propagation of incident light, for example along $\hat{z}$, considering time reversal symmetry and energy conservation, we can write,

$$\epsilon = \begin{pmatrix} \epsilon_{xx} & \epsilon_{xy}(B) & 0 \\ -\epsilon_{xy}(B) & \epsilon_{yy} & 0 \\ 0 & 0 & \epsilon_{zz} \end{pmatrix} \tag{3.6}$$

The normalized eignemodes of ϵ are given by

$$\begin{pmatrix} E_x \\ E_y \end{pmatrix}_{\pm} = \frac{1}{\sqrt{2}} \begin{pmatrix} 1 \\ \pm i \end{pmatrix} \tag{3.7}$$

Here E_x and E_y are the electric fields along x and y direction. The eigen values of the above matrix are $\epsilon_{xx} \pm i\epsilon_{xy}(B)$ with eigen vectors [1, i] and [1, -i]. These eigen vectors correspond to right and left circularly polarized light, which shows that circularly polarized light will remain circularly polarized after interacting with the material having the above permitivity tensor. Refractive indices for circularly polarized light would be $n_+ = \sqrt{(\epsilon_{xx} + i\epsilon_{xy})}$ and $n_- = \sqrt{(\epsilon_{xx} - i\epsilon_{xy})}$. This implies that for circularly polarized light, different helicities will experience different speed in the material which will introduce a phase delay. For linearly polarized light, it will introduce polarization rotation, but light at the exit of the media will remain linearly polarized.

3.2.1 Faraday effect

In the Faraday effect [14, 17], the polarization of light which is transmitted through magnetic materials is rotated. Following the analysis discussed for the case of isotropic media with permittivity tensor given by equation 3.6, the Faraday rotation (θ_F) of light propagating through magnetic media is given by [15]

$$\theta_F = \frac{\omega}{2c}(n_+ - n_-)L \tag{3.8}$$

where ω is the angular frequency of the light, L is the length travelled by the light in the magnetic medium and n_+ and n_- are refractive indices for right handed and left handed

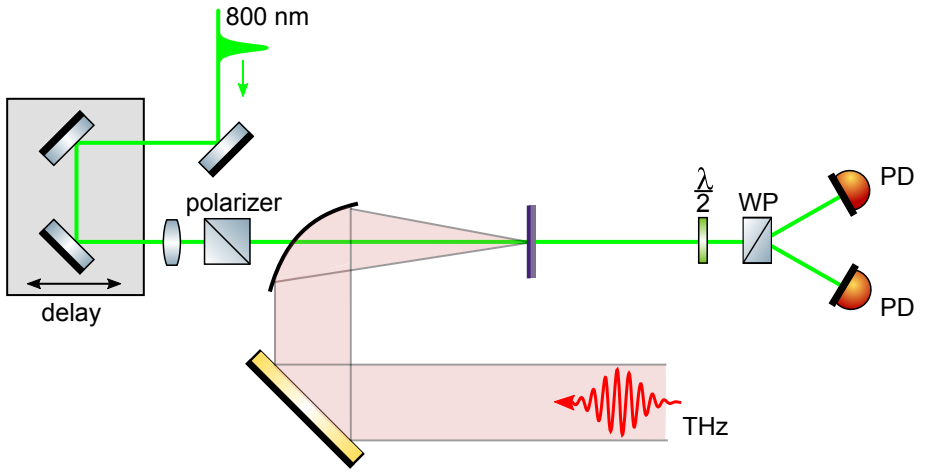

FIGURE 3.2: Schematic of the Faraday set-up used in this thesis. The THz pump (shown in red) is incident on the material under investigation at normal incidence. 100 femtosecond 800 nm NIR laser pulses (shown in green) are collinear with the THz pump. The transient change in magnetization of the materials is probed with the polarization rotation of the 800 nm NIR laser pulse passing through the material. $\frac{\lambda}{2}$, WP, and PD stand for the half-wave plate for 800 nm wavelength, a Wollaston prism and the photo-diodes, respectively.

circular polarization of light. If the light propagates through a magnetic medium with non zero absorption coefficient, i.e., the absorption is different for right handed and left handed circular polarization then polarization is changed from linear to elliptical. The schematic of THz pump NIR Faraday probe is shown in the figure 3.2.

3.2.2 Magneto-optical Kerr effect (MOKE)

In the Kerr effect [15] the polarization of the reflected light from the sample surface changes. This change is proportional to the internal magnetization of the sample. The Kerr effect can be measured in three different geometries as shown in the figure 3.3.

In the polar MOKE configuration, the magnetization of the medium is pointing out of the plane. The NIR probe pulses can be perpendicular to the sample surface and one observes the change in out-of-plane magnetization by measuring the changes of probe pulse polarization state. For normal incidence, the analytical expression for the Kerr-rotation angle is given by [19],

$$\theta_{pol} = \frac{\epsilon_{xy}}{\sqrt{\epsilon_{xx}}(\epsilon_{xx} - 1)} \tag{3.9}$$

In longitudinal and transverse MOKE, the magnetization of sample lies in the plane of the sample. For longitudinal MOKE, the magnetization of the sample is parallel to the plane of incidence while for transverse MOKE it is perpendicular to the plane of

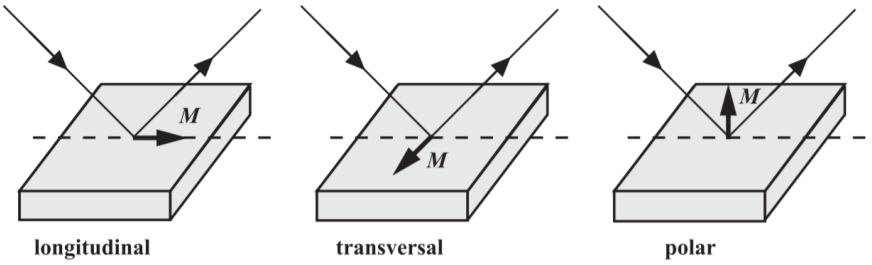

FIGURE 3.3: Different configurations for measurement of Kerr effect [18]. Longitudinal and transverse MOKE geometry allows to probe the magnetization which is in plane, whereas polar MOKE geometry allows to probe magnetization which is out of plane.

incidence. For polar and longitudinal MOKE, there is always a non-zero component of magnetization on the wave vector of the probe pulses, which results in the rotation of polarization.

The magnitude of the Kerr effect depends on the geometry and the angle of incidence. The largest effect is observed with polar MOKE geometry with probe pulses being perpendicular to the sample surface. The schematic of the polar MOKE geometry used is shown in figure 3.4.

3.3 Light sources

3.3.1 Near infra-red (NIR) femtosecond laser sources

The femtosecond laser systems used in the laboratory consist of a Ti-sapphire Vitara-T oscillator, a regenerative amplifier (RegA) system and a Legend Elite amplifier system from Coherent. The oscillator laser system is pumped by Verdi18 solid state continuous laser system. The VitaraT oscillator [20] produces short laser pulses centered around 800 nm with a bandwidth of 30-120 nm and repetition rate of 78 MHz with average power $>$ 450 mW.

The oscillator pulses are then used to seed RegA and Legend amplifiers. The purpose of the amplifier is to enhance the energy per pulse by few orders of magnitude. The RegA [21] has an output of 5 μJ at 200 KHz with a repetition rate that can be varied from 100

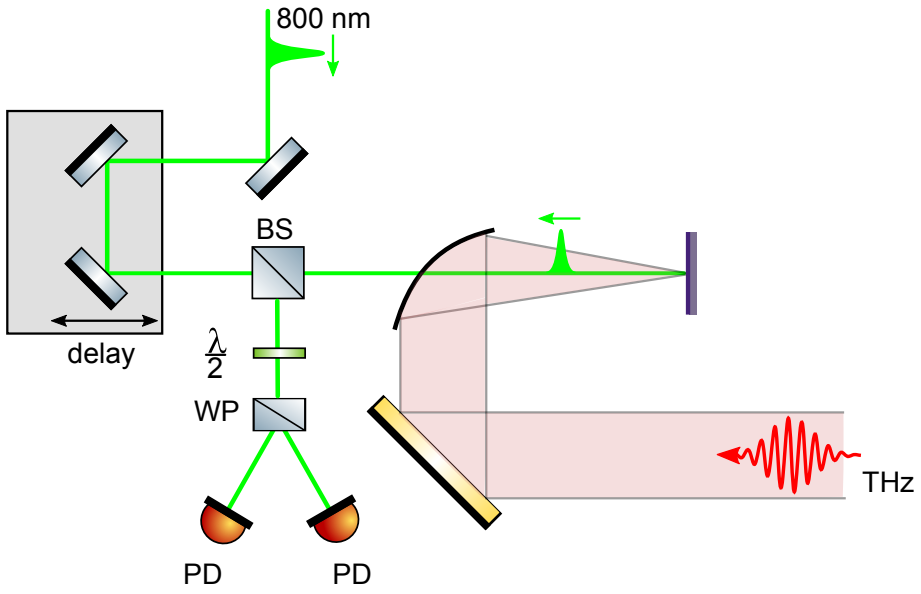

FIGURE 3.4: Schematic of the polar MOKE set-up used in this thesis. The THz pump (shown in red) is incident on the material under investigation at normal incidence. 100 femtosecond 800 nm NIR laser pulses (shown in green) are collinear with the THz pump. The transient change in magnetization is probed with the change in the polarization of the 800 nm NIR laser pulse reflected back from the material. $\frac{\lambda}{2}$, WP, and PD stand for the half-wave plate for 800 nm wavelength, a Wollaston prism and the photo-diodes, respectively.

KHz to 250 KHz with a 100 fs pulse duration. On the other hand, the Legend Elite[22] has a 1 mJ pulse energy at repetition rate of 1 KHz with a 100 fs pulse duration.

3.3.2 Laser-based THz light sources

The readily available table-top laser-based THz sources and their detection schemes [23–25] have helped to gain understanding of the physics in the THz frequency regime. THz time domain spectroscopy has been extensively used to probe low energy excitations in materials, liquids and gases [26–30]. Recent advancements in high electric field amplitude THz sources have opened up a new branch of fundamental science where high-field THz sources have been used to excite and control the low-energy excitations in a coherent fashion [4, 23, 31–38].

The typical laser-based THz sources used in laboratories are based on the optical rectification process using intense near infra-red (NIR) fs laser systems, see figure 3.5. Optical rectification is based on a second order nonlinear process which can be seen as difference frequency generation. When a fs laser pulse is incident on a material, electrons move back and forth following the electric field of the laser pulse. In case of materials with broken symmetry, excited electrons and ions undergo additional displacement caused by polarization ($P_r(t)$) which follows the intensity envelope of the laser pulse. This rectified

motion of charge carriers emits electromagnetic radiation which has a bandwidth of $\sim \frac{1}{\tau}$, where τ is the laser pulse duration in femtoseconds, corresponding to frequencies in the few THz regime.

According to Maxwells equations, the polarization $\boldsymbol{P}$ acts as a source term, radiating off a single cycle electro-magnetic pulse in the far field.

$$\Delta \times \Delta \times \boldsymbol{E} + \frac{1}{c^2}\frac{\delta^2}{\delta t^2}(\epsilon \boldsymbol{E}) = -\frac{4\pi}{c^2}\frac{\delta^2 \boldsymbol{P}}{\delta t^2} \tag{3.10}$$

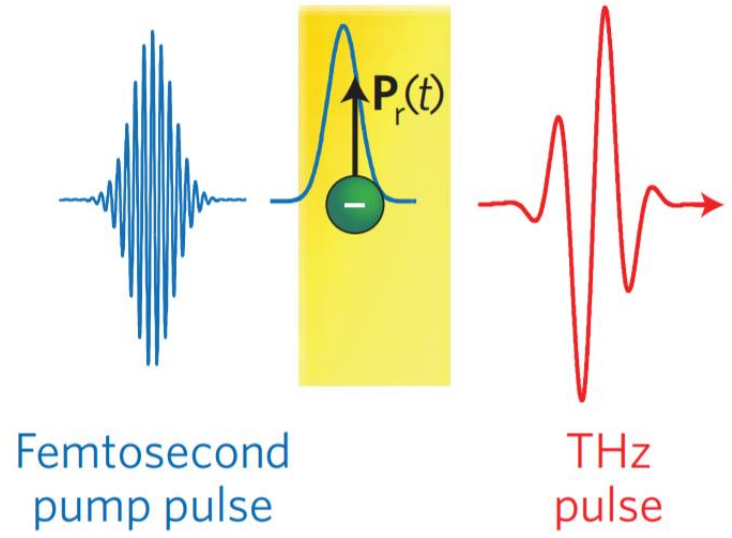

FIGURE 3.5: Schematic of the optical rectification process for THz generation, adapted from [4]. An intense femtosecond pulse is incident on a non-inversion symmetric crystal. This femtosecond pulse induces a charge displacement, which follows the envelope of the femtosecond pulse. This charge displacement acts as a source of THz generation from the non-inversion symmetric crystal.

In order to have a high efficiency of THz generation, the laser pulse and generated THz should travel at the same speed in the crystal. In such a situation, THz waves can add up coherently throughout the length of the crystal. This is known as the phase matching condition, which requires a crystal where the group refractive index for the femtosecond laser pulse is equal to the phase refractive index for the THz:

$$n_{gr}^{vis} = n_{ph}^{THz} \tag{3.11}$$

The most commonly used materials for THz generation are ZnTe, GaP, $LiNbO_3$, DAST. The phase matching of optical group velocity and THz phase velocity is essential for efficient THz generation. Such phase matching can be achieved in collinear fashion with

materials such as ZnTe, GaP. To further increase the efficiency of THz generation one needs materials with higher dielectric constants, such as $LiNbO_3$, that offers a higher elector-optic coefficient. In such materials, collinear phase matching cannot be achieved collinearly [39]. For such cases, tilted pulse-front schemes for $LiNbO_3$ using gratings can be used as demonstrated [40]. The advantage of this technique over collinear phase matching THz emission is the scalabilty of emitted THz power with pump power and spot size of the pump [41].

In this thesis, a 800 nm NIR laser pump at 1 KHz repetition rate has been used for THz generation using a tilted wave-front. The average laser pump power used was $\sim$ 1W and emitted THz power is of the order of a few mW. Thus, the conversion efficiency for tilted pulse-front THz generation is roughly 10^{-3}. The typical waveform of the THz emission using tilted pulse-front generation and its Fourier spectrum is shown in the figure 3.6.

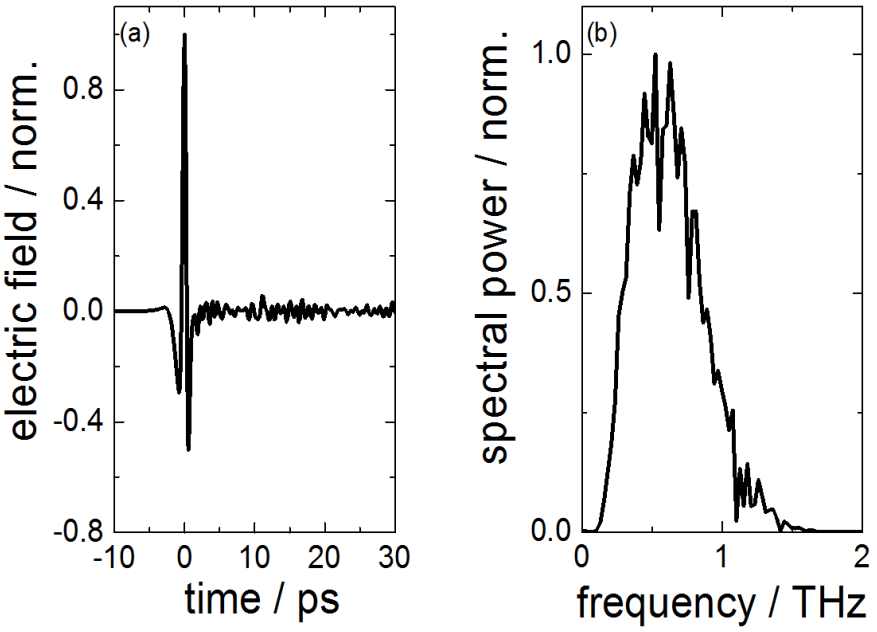

FIGURE 3.6: Typical time trace along with its frequency spectrum of generated THz radiation using LN as a THz source. (a) time domain trace of the electric field of generated THz radiation, (b) shows the frequency spectrum of the recorded time scan.

3.3.3 TELBE

In the experiments where multi-cycle, narrow-band and spectrally dense THz pulses are required, the TELBE facility is used. The TELBE facility has two different THz sources: i) tunable THz radiation based on a magnetic undulator and ii) broadband coherent diffraction radiation. The THz radiation is generated from electron bunches accelerated in superconducting radio frequency (SRF) cavities. The emission from the

accelerated electron bunches is based on the principle of super-radiance. The super-radiance radiation is emitted when the area of emitters become significantly smaller than the wavelength of radiation. For the electron bunch duration (τ), the frequency of superradiant emission is given by the inverse of τ. Figure 3.7 shows the schematic of the superradiant process. When the electron bunch has a width larger than the wavelength of the radiation then one gets the incoherent radiation, where the intensity of the radiation is proportional to the number of electrons. In contrast, when the electron bunch has a width smaller or comparable to the wavelength of the radiation then a superradiant process is observed. For a superradiant process, the intensity of the emission is proportional to the square of the electron number N.

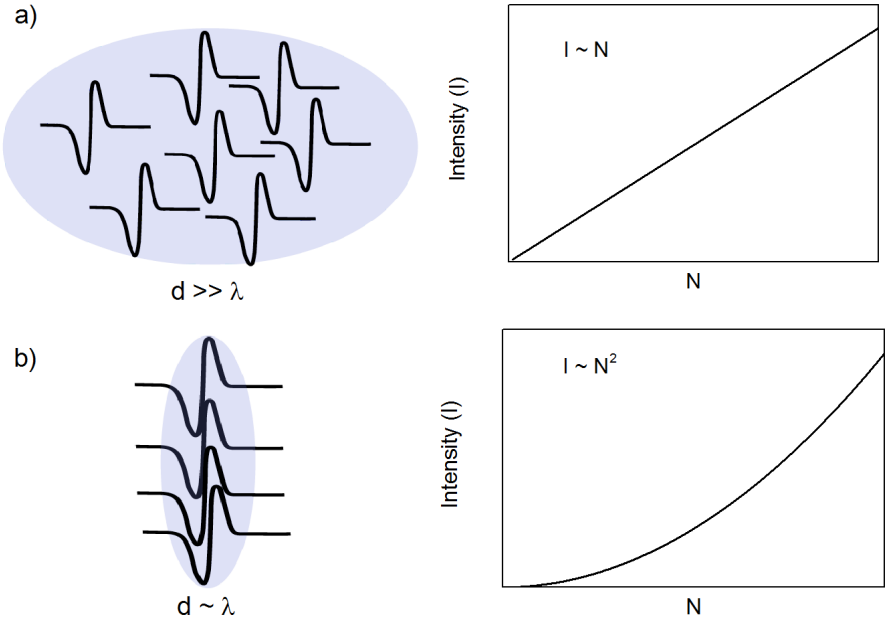

FIGURE 3.7: Schematic representing the concept of superradiant emission from an electron bunch. (a) when the electron bunch width is larger than the wavelength of emitted radiation, incoherent radiation is observed (b) when the electron bunch width becomes comparable to the wavelength of the radiation then superradiant emission with square law is observed.

TELBE has an advantage over conventional laser-based table top THz sources because of its high spectral density and frequency tunability. Figure 3.8a shows the maximum pulse energy for the TELBE source. Figure 3.8a shows the comparison between laser-based sources (black dots) and the TELBE source. Laser-based sources operating higher than 10 kHz repetition rate are limited to pulse energies less than 10 nJ [42, 43], whereas for repetition rates above 250 kHz it can produce 0.25 nJ pulse energies [44, 45]. TELBE currently exceeds these values by more than 2 orders of magnitude (blue shaded) with 100 pC electron bunches. Electron bunches with 1 nC result in pulse energies of 100 μJ (light-blue-shaded). A high repetition rate also provides an exceptional dynamic range required for better detection statistics. Figure 3.8b shows the maximum observed pulse

energy as a function of frequency at TELBE (red dots) with 100 kHz repetition rate and 100 pC electron bunches. The pulse energies exceed the currently most intense high-repetition rate laser-based sources (shaded) by up to 2 orders of magnitude. It should be noted that, the laser-based sources are broadband and have a distribution of spectral weight over many frequencies as indicated by the color tone in the respective shaded areas in figure 3.8b. Experiments aimed at driving a narrow-band low frequency excitation resonantly thereby benefit additionally from the considerably higher spectral density. A novel pulse-resolved data acquisition system facilitates a timing accuracy between TELBE and NIR laser systems of 12 fs (rms) and an exceptional dynamic range of 10^6 or better in experiments [46].

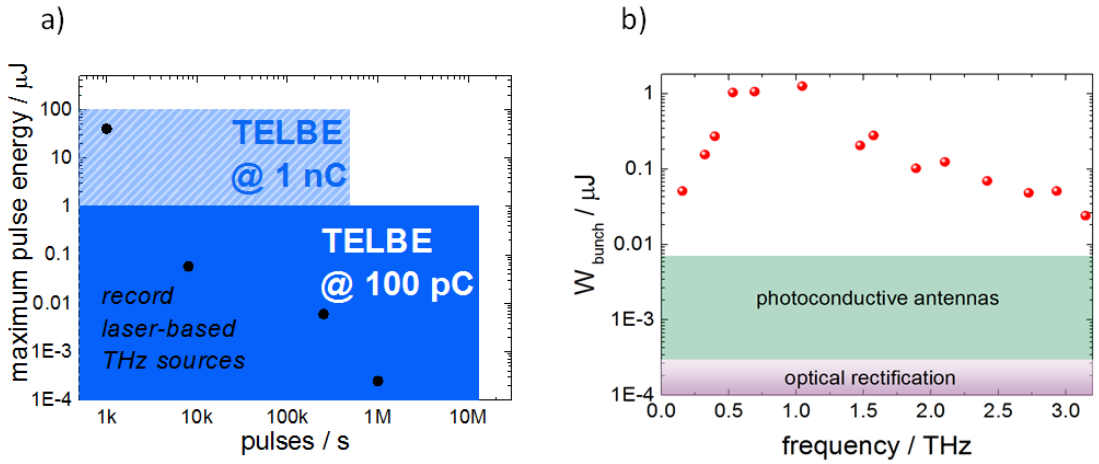

FIGURE 3.8: Maximum pulse energy observed at TELBE as a function of repetition rate, for a given THz frequency. Adapted from [47] (a) Maximum pulse energy at TELBE as a function of repetition rate. With 100 pC electron bunches, TELBE pulse energy is 2 orders of magnitude higher than from intense table top THz sources at the same repetition rate of 100 kHz. (b) maximum pulse energy at TELBE as a function of THz frequency, observed at 100 KHz repetition rate and 100 pC electron bunches.

TELBE currently operates at 100 KHz repetition rate with the THz frequencies that can be tuned from 0.1 THz to 2 THz with a 20 % bandwidth [47], see figure 3.9. The pulse energy of the THz pulses is up to 2 μJ. Figure 3.9 shows the wave-forms and the spectra of the undulator-based THz emission for the TELBE facility. The polarization of the THz radiation is linear but can be controlled between circular and elliptical by means of appropriate wave plates. All the experiments using TELBE, included in this thesis, were done with 800 nm probe pulses from RegA.

3.4 Bibliography

[1] X.-C. Zhang, B. Hu, J. Darrow, and D. Auston, "Generation of femtosecond electromagnetic pulses from semiconductor surfaces," *Applied Physics Letters*, vol. 56,

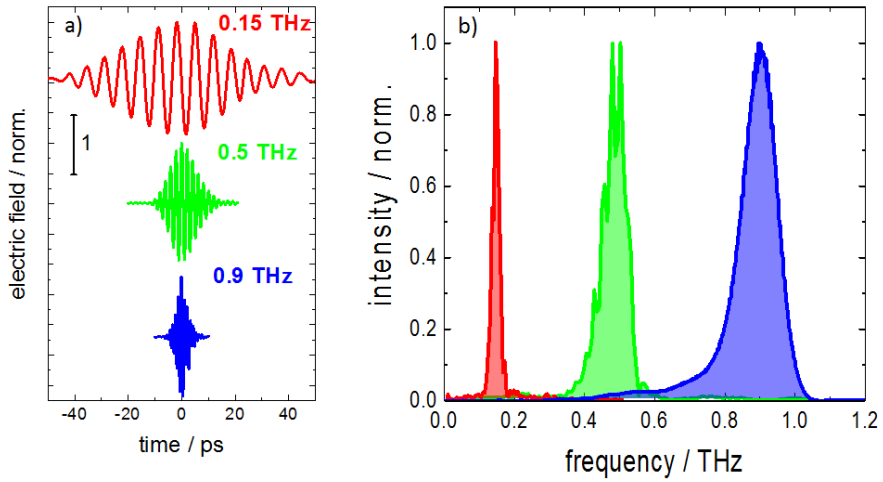

FIGURE 3.9: Frequency tunability of TELBE source. (a) Electric field wave-forms for different THz frequencies (b) normalized intensity spectrum for the THz frequencies shown in (a).

no. 11, pp. 1011–1013, 1990.

[2] E. Beaurepaire, G. Turner, S. Harrel, M. Beard, J.-Y. Bigot, and C. Schmuttenmaer, "Coherent terahertz emission from ferromagnetic films excited by femtosecond laser pulses," *Applied Physics Letters*, vol. 84, no. 18, pp. 3465–3467, 2004.

[3] D. J. Hilton, R. Averitt, C. Meserole, G. L. Fisher, D. J. Funk, J. D. Thompson, and A. J. Taylor, "Terahertz emission via ultrashort-pulse excitation of magnetic metal films," *Optics letters*, vol. 29, no. 15, pp. 1805–1807, 2004.

[4] T. Kampfrath, K. Tanaka, and K. A. Nelson, "Resonant and nonresonant control over matter and light by intense terahertz transients," *Nature Photonics*, vol. 7, no. 9, p. 680, 2013.

[5] T. H. Kim, S. Y. Hamh, J. W. Han, C. Kang, C.-S. Kee, S. Jung, J. Park, Y. Tokunaga, Y. Tokura, and J. S. Lee, "Coherently controlled spin precession in canted antiferromagnetic YFeO3 using terahertz magnetic field," *Applied Physics Express*, vol. 7, no. 9, p. 093007, 2014.

[6] Z. Jin, Z. Mics, G. Ma, Z. Cheng, M. Bonn, and D. Turchinovich, "Single-pulse terahertz coherent control of spin resonance in the canted antiferromagnet YFeO3, mediated by dielectric anisotropy," *Physical Review B*, vol. 87, no. 9, p. 094422, 2013.

[7] J. Nishitani, K. Kozuki, T. Nagashima, and M. Hangyo, "Terahertz radiation from coherent antiferromagnetic magnons excited by femtosecond laser pulses," *Applied Physics Letters*, vol. 96, no. 22, p. 221906, 2010.

[8] D. J. Griffiths, "Electrodynamics," *Introduction to Electrodynamics, 3rd ed., Prentice Hall, Upper Saddle River, New Jersey*, pp. 301–306, 1999.

[9] S. Hooker and C. Webb, *Laser Physics*. Oxford Master Series in Physics, Oxford University Press, 2010.

[10] Q. Wu and X.-C. Zhang, "Free-space electro-optic sampling of terahertz beams," *Applied Physics Letters*, vol. 67, no. 24, pp. 3523–3525, 1995.

[11] Q. Wu and X.-C. Zhang, "Ultrafast electro-optic field sensors," *Applied physics letters*, vol. 68, no. 12, pp. 1604–1606, 1996.

[12] A. Nahata, A. S. Weling, and T. F. Heinz, "A wideband coherent terahertz spectroscopy system using optical rectification and electro-optic sampling," *Applied physics letters*, vol. 69, no. 16, pp. 2321–2323, 1996.

[13] C. Winnewisser, P. U. Jepsen, M. Schall, V. Schyja, and H. Helm, "Electro-optic detection of thz radiation in LiTaO3, LiNbO3 and ZnTe," *Applied Physics Letters*, vol. 70, no. 23, pp. 3069–3071, 1997.

[14] P. Schatz and A. McCaffery, "The faraday effect," *Quarterly Reviews, Chemical Society*, vol. 23, no. 4, pp. 552–584, 1969.

[15] A. K. Zvezdin and V. A. Kotov, *Modern magnetooptics and magnetooptical materials*. CRC Press, 1997.

[16] P. N. Argyres, "Theory of the faraday and kerr effects in ferromagnetics," *Physical Review*, vol. 97, no. 2, p. 334, 1955.

[17] H. S. Bennett and E. A. Stern, "Faraday effect in solids," *Physical Review*, vol. 137, no. 2A, p. A448, 1965.

[18] M. Djordjević Kaufmann, "Magnetization dynamics in all-optical pump-probe experiments: spin-wave modes and spin-current damping," *Ph.D. Thesis, Georg-August-Universität Göttingen*, 2007.

[19] A. K. Zvezdin and V. A. Kotov, *Modern magnetooptics and magnetooptical materials*. Institute of Physics Pub., 1997.

[20] C. V. D. Sheet, "*Vitara*." `https://edge.coherent.com/assets/pdf/COHR_Vitara_DS_0416revC_3.pdf`.

[21] C. R. D. Sheet, "*RegA 9000*." `https://cohrcdn.azureedge.net/assets/pdf/RegA-Data-Sheet.pdf`.

[22] C. L. D. Sheet, "*Legend*." https://cohrcdn.azureedge.net/assets/pdf/LegendEliteHEplus_DS_0715revA_6.pdf.

[23] H. Y. Hwang, S. Fleischer, N. C. Brandt, B. G. Perkins Jr, M. Liu, K. Fan, A. Sternbach, X. Zhang, R. D. Averitt, and K. A. Nelson, "A review of non-linear terahertz spectroscopy with ultrashort tabletop-laser pulses," *Journal of Modern Optics*, vol. 62, no. 18, pp. 1447–1479, 2015.

[24] R. Ulbricht, E. Hendry, J. Shan, T. F. Heinz, and M. Bonn, "Carrier dynamics in semiconductors studied with time-resolved terahertz spectroscopy," *Reviews of Modern Physics*, vol. 83, no. 2, p. 543, 2011.

[25] H. J. Joyce, J. L. Boland, C. L. Davies, S. A. Baig, and M. B. Johnston, "A review of the electrical properties of semiconductor nanowires: insights gained from terahertz conductivity spectroscopy," *Semiconductor Science and Technology*, vol. 31, no. 10, p. 103003, 2016.

[26] W. L. Chan, J. Deibel, and D. M. Mittleman, "Imaging with terahertz radiation," *Reports on progress in physics*, vol. 70, no. 8, p. 1325, 2007.

[27] M. Van Exter and D. Grischkowsky, "Optical and electronic properties of doped silicon from 0.1 to 2 THz," *Applied Physics Letters*, vol. 56, no. 17, pp. 1694–1696, 1990.

[28] C. A. Schmuttenmaer, "Exploring dynamics in the far-infrared with terahertz spectroscopy," *Chemical reviews*, vol. 104, no. 4, pp. 1759–1780, 2004.

[29] B. Yu, F. Zeng, Y. Yang, Q. Xing, A. Chechin, X. Xin, I. Zeylikovich, and R. Alfano, "Torsional vibrational modes of tryptophan studied by terahertz time-domain spectroscopy," *Biophysical Journal*, vol. 86, no. 3, pp. 1649–1654, 2004.

[30] B. Yu, Y. Yang, F. Zeng, X. Xin, and R. Alfano, "Terahertz absorption spectrum of D2O vapor," *Optics communications*, vol. 258, no. 2, pp. 256–263, 2006.

[31] T. Kampfrath, A. Sell, G. Klatt, A. Pashkin, S. Mährlein, T. Dekorsy, M. Wolf, M. Fiebig, A. Leitenstorfer, and R. Huber, "Coherent terahertz control of antiferromagnetic spin waves," *Nature Photonics*, vol. 5, no. 1, p. 31, 2011.

[32] W. Hu, S. Kaiser, D. Nicoletti, C. R. Hunt, I. Gierz, M. C. Hoffmann, M. Le Tacon, T. Loew, B. Keimer, and A. Cavalleri, "Optically enhanced coherent transport in YBa2Cu3O6.5 by ultrafast redistribution of interlayer coupling," *Nature materials*, vol. 13, no. 7, p. 705, 2014.

[33] S. Kaiser, C. R. Hunt, D. Nicoletti, W. Hu, I. Gierz, H. Liu, M. Le Tacon, T. Loew, D. Haug, B. Keimer, *et al.*, "Optically induced coherent transport far above T_c in underdoped $YBa_2Cu_3O_{6+\delta}$," *Physical Review B*, vol. 89, no. 18, p. 184516, 2014.

[34] S. Kaiser, S. Clark, D. Nicoletti, G. Cotugno, R. Tobey, N. Dean, S. Lupi, H. Okamoto, T. Hasegawa, D. Jaksch, *et al.*, "Optical properties of a vibrationally modulated solid state mott insulator," *Scientific reports*, vol. 4, p. 3823, 2014.

[35] M. Liu, H. Y. Hwang, H. Tao, A. C. Strikwerda, K. Fan, G. R. Keiser, A. J. Sternbach, K. G. West, S. Kittiwatanakul, J. Lu, *et al.*, "Terahertz-field-induced insulator-to-metal transition in vanadium dioxide metamaterial," *Nature*, vol. 487, no. 7407, p. 345, 2012.

[36] A. Pashkin, A. Sell, T. Kampfrath, and R. Huber, "Electric and magnetic terahertz nonlinearities resolved on the sub-cycle scale," *New Journal of Physics*, vol. 15, no. 6, p. 065003, 2013.

[37] M. Rini, N. Dean, J. Itatani, Y. Tomioka, Y. Tokura, R. W. Schoenlein, A. Cavalleri, *et al.*, "Control of the electronic phase of a manganite by mode-selective vibrational excitation," *Nature*, vol. 449, no. 7158, p. 72, 2007.

[38] D. Fausti, R. I. Tobey, N. Dean, S. Kaiser, A. Dienst, M. C. Hoffmann, S. Pyon, T. Takayama, H. Takagi, and A. Cavalleri, "Light-induced superconductivity in a stripe-ordered cuprate," *Science*, vol. 331, p. 189, 2011.

[39] K.-L. Yeh, M. Hoffmann, J. Hebling, and K. A. Nelson, "Generation of 10 μ j ultrashort terahertz pulses by optical rectification," *Applied Physics Letters*, vol. 90, no. 17, p. 171121, 2007.

[40] J. Hebling, G. Almasi, I. Z. Kozma, and J. Kuhl, "Velocity matching by pulse front tilting for large-area thz-pulse generation," *Optics Express*, vol. 10, no. 21, pp. 1161–1166, 2002.

[41] A. Stepanov, J. Hebling, and J. Kuhl, "Generation, tuning, and shaping of narrow-band, picosecond thz pulses by two-beam excitation," *Optics Express*, vol. 12, no. 19, pp. 4650–4658, 2004.

[42] S.-W. Huang, E. Granados, W. R. Huang, K.-H. Hong, L. E. Zapata, and F. X. Kärtner, "High conversion efficiency, high energy terahertz pulses by optical rectification in cryogenically cooled lithium niobate," *Optics letters*, vol. 38, no. 5, pp. 796–798, 2013.

[43] M. Kunitski, M. Richter, M. D. Thomson, A. Vredenborg, J. Wu, T. Jahnke, M. Schöffler, H. Schmidt-Böcking, H. G. Roskos, and R. Dörner, "Optimization of

single-cycle terahertz generation in LiNbO3 for sub-50 femtosecond pump pulses," *Optics Express*, vol. 21, no. 6, pp. 6826–6836, 2013.

[44] M. Beck, H. Schäfer, G. Klatt, J. Demsar, S. Winnerl, M. Helm, and T. Dekorsy, "Impulsive terahertz radiation with high electric fields from an amplifier-driven large-area photoconductive antenna," *Optics Express*, vol. 18, no. 9, pp. 9251–9257, 2010.

[45] M. C. Hoffmann, K.-L. Yeh, H. Y. Hwang, T. S. Sosnowski, B. S. Prall, J. Hebling, and K. A. Nelson, "Fiber laser pumped high average power single-cycle terahertz pulse source," *Applied Physics Letters*, vol. 93, no. 14, p. 141107, 2008.

[46] S. Kovalev, B. Green, T. Golz, S. Maehrlein, N. Stojanovic, A. Fisher, T. Kampfrath, and M. Gensch, "Probing ultra-fast processes with high dynamic range at 4th-generation light sources: Arrival time and intensity binning at unprecedented repetition rates," *Structural Dynamics*, vol. 4, no. 2, p. 024301, 2017.

[47] B. Green, S. Kovalev, V. Asgekar, G. Geloni, U. Lehnert, T. Golz, M. Kuntzsch, C. Bauer, J. Hauser, J. Voigtlaender, *et al.*, "High-field high-repetition-rate sources for the coherent THz control of matter," *Scientific reports*, vol. 6, p. 22256, 2016.